High-entropy oxide $(CeGdHfPrZr)O_2$ nanoparticles as reusable photocatalyst for wastewater remediation

Mariappan Anandkumar[a*], Kannan P.K.[b], Shanmugavel Sudarsan[a], Trofimov E.A.[a]

[a]South Ural State University, Chelyabinsk 454080, Russian Federation

[b] Department of Physics, PSG Institute of Technology and Applied Research, Coimbatore 641 062, India

Highlights:

- Single-Phase $(CeGdHfPrZr)O_2$ was synthesized using a hydrothermal technique.
- $(CeGdHfPrZr)O_2$ showed better photocatalytic activity at alkaline pH values.
- Hydroxyl radical is responsible for MB degradation.
- Better photocatalytic recyclability is observed without any phase transformation.
- $(CeGdHfPrZr)O_2$ appears to be an attractive photocatalytic material for wastewater remediation.

Abstract:

High-entropy materials (HEM) play a significant role in current scientific research and are characterized by their complexity, which makes them the next generation of nanomaterials. The present study investigates the synthesis of $(CeGdHfPrZr)O_2$ high-entropy oxide nanoparticles using a hydrothermal technique. Various characterization techniques, such as X-ray diffraction (XRD), and scanning electron microscopy (SEM) were used to investigate the structural properties, while UV-visible spectroscopy was used to investigate the optical properties. The results indicate the formation of a single-phase cubic fluorite-high-entropy

*Corresponding author. Tel: +91-741-861-6336. E-mail: drmaksmile@gmail.com

oxide system with a mean crystallite size of 5.4 nm. The optical bandgap of (CeGdHfPrZr)O_2 nanoparticles is found to be 2.01 eV. The photocatalytic activity of the synthesized oxide nanoparticles was assessed using methylene blue (MB) dye as a model pollutant. In the current study, we examined and discussed the effect of various photocatalytic parameters on the degradation of MB dye. The results showed that the (CeGdHfPrZr)O_2 nanoparticles had high photocatalytic activity and were found to be dependent on various parameters. A higher photocatalyst concentration impedes the degradation kinetics and, as a result, limits photon penetration into the reaction solution. Similarly, increased hydroxyl radical generation at a basic pH improved MB dye degradation. In addition, based on the band positions and radical scavenging study, hydroxyl radicals are responsible for the degradation of dye. (CeGdHfPrZr)O_2 nanoparticles can be used as a promising catalyst for the photocatalytic degradation of organic pollutants.

Keywords:

High-entropy oxide; Solid solution; Photocatalyst; Methylene Blue; Structural stability

1. Introduction:

Research on a new class of nanomaterials referred to as "High-entropy materials" (HEM) has received considerable attention in recent years. A HEM system is unlikely to differ from a conventional doped system in many aspects. Typically, HEMs are formed by combining five or more principal elements to achieve complete solubility and, as a result, form a solid solution. Therefore, HEMs are extremely stable and versatile, which makes them suitable for a wide range of applications. This in turn contributes to the creation of a new paradigm in scientific research regarding HEMs to create materials with unique physical and chemical properties [1-3]. High-entropy oxide (HEO) is one of the most intriguing systems that have been shown to exhibit better thermal properties [4, 5], optical [6], photoluminescence [7], dielectric [8, 9],

thermoelectric [10], magnetic [11-13], etc. $TiZrNbHfTaO_{11}$ oxide, for example, outperformed typical photocatalysts such as anatase TiO_2 and $BiVO_4$, and was comparable to P25 TiO_2 in terms of photocatalytic CO_2 conversion [14]. Furthermore, $Pr_{1/6}La_{1/6}Nd_{1/6}Ba_{1/6}Sr_{1/6}Ca_{1/6}CoO_{3-\delta}$ is reported as a high-performance bifunctional air electrode for reversible proton ceramic electrochemical cell compared to advanced air electrodes reported so far[15]. These findings demonstrate the advantages of designing high-entropy materials in comparison to pure or doped oxide system.

Moreover, their tuneable structural and chemical properties make them ideal for use in a wide range of practical applications, including energy storage [8, 16], sensors [17-19], thermal barrier coatings [20], catalysis [21], electrocatalysts [22], and photocatalysts [6, 23]. Despite the attention given to other functional applications, few research has been conducted on using HEO in the field of photocatalysis, thus leaving the area largely unexplored. Edalati *et al.* produced a $TiZrNbTaWO_{12}$ photocatalyst for studying the oxygen evolution reaction [24]. Yu *et al.* studied the photocatalytic reduction of Cr(VI) using $A_{32}Ti_8Sn_8Nb_4Ta_4Me_8O_{96}$ (A=Ba, Sr; Me=Fe, Ga) perovskite structure and found that the system containing Fe has the best photocatalytic activity [25]. Anandkumar *et al.* studied the photocatalytic conversion of Cr(VI) and degradation of methylene blue using $Gd_{0.2}La_{0.2}Ce_{0.2}Hf_{0.2}Zr_{0.2}O_2$ and $Gd_{0.2}La_{0.2}Y_{0.2}Hf_{0.2}Zr_{0.2}O_2$ high-entropy oxide. Both the oxide systems display good Cr(VI) reduction and better methylene blue degradation [6].

Considering the significant gap left in the field of high-entropy photocatalysts, wastewater remediation is of particular interest to us. A competitive economic race has led to rapid industrialization, which in turn has resulted in an increase in wastewater discharge [26-29]. Despite the existence of strict regulations, the possibility of industrial effluents contaminating fresh water remains uncontrollable, and serious action must be pursued. An increase in monitoring and enforcement efforts, as well as improvements in wastewater treatment

processes, may be necessary to reduce water pollution. Various contaminants such as methyl orange, methylene blue, and other heavy metals such as Cr, Cd, Hg, etc. have been discharged from different industries like leather, textiles, mining, cosmetics, etc[6]. The textile and paper industries use more than 10,000 synthetic dyes and pigments, causing significant negative environmental and health impacts[27]. Water bodies are at risk from the direct discharge of industrial effluents which pose serious ecotoxicological threats. Several health issues for human beings as well as for wildlife as a result of ingesting contaminated water have been identified [6]. In order to protect humans and wildlife, it is imperative to reduce the amount of these pollutants in our environment.

To neutralize the harmful chemicals, present in wastewater discharge, the advanced oxidation process (AOP) through heterogeneous photocatalysis is one of the most viable and eco-friendly techniques for eliminating industrial dyes using reactive oxygen species (ROS) [30, 31]. The photocatalytic action is usually carried out using either natural sunlight or a UV/visible light source that generates an electron-hole pair on the photocatalyst surface [32]. This leads to the generation of high levels of ROS, which are responsible for neutralizing dye molecules. The AOP process is cost-effective, and efficient and the degradation product resulting from this process is least harmful to the environment and soil. Sudarsan *et al.* synthesized a copper ferrite nanocomposite by solvothermal technique from discarded printed circuit boards and used it as a photocatalyst for the degradation of Congo red dye. The prepared copper ferrite nanocomposite could effectively decompose 96.19% of dye within 120 min [33]. Doped systems such as Sr doped $BaTiO_3$ show better performance for the degradation of rhodamine B with a degradation rate of 92.66 % within 18 min[34].

Similarly, several heterojunctions have been explored in order to degrade methylene blue and toxic metals such as Cr(VI) [35-38]. A number of nanomaterials have been reported to degrade different dyes [34, 39]. Ceria-based nanocomposite ($Ce_{0.8}Y_{0.2}O_{2-\delta}$–$Ce_{0.8}Sm_{0.2}O_{2-\delta}$)

nanoparticles fabricated by the chemical co-precipitation technique show a degradation efficiency of 93%. Similarly, NiO-$Ce_{0.9}Y_{0.1}O_{2-\delta}$–$Ce_{0.9}Sm_{0.1}O_{2-\delta}$ nanoparticle photocatalyst was used to degrade congo red dye[40]. As a result, we investigate a new photocatalytic material for the degradation of methylene blue dye to ensure the environmental effects can be minimized.

To fill this gap, our scientific work seeks to develop new high-entropy photocatalysts that can effectively remove contaminants from wastewater. In this present study, we have synthesized $(CeGdHfPrZr)O_2$ nanoparticles using a hydrothermal route using NaOH and Polyvinylpyrrolidone. Further, we have investigated the photocatalytic activity of $(CeGdHfPrZr)O_2$ nanoparticles for the photocatalytic degradation of methylene blue dye. An in-depth investigation of the photocatalytic degradation of MB dye has been carried out by varying different photocatalytic parameters and is discussed in detail. As a result of this study, we may be able to reveal novel applications for HEOs in the area of photocatalysis.

2. Experimental section

2.1. Materials and reagents

Cerium (III) nitrate hexahydrate ($Ce(NO_3)_3•6H_2O$), zirconium (IV) nitrate dihydrate ($Zr(NO_3)_2•2H_2O$), hafnium (IV) oxychloride ($HfOCl_2•8H_2O$), gadolinium (III) nitrate hexahydrate ($Gd(NO_3)_3•6H_2O$), praseodymium (III) nitrate hexahydrate ($Pr(NO_3)_3•6H_2O$), methylene blue, hydrogen peroxide (H_2O_2), hydrochloric acid (HCl), sodium hydroxide (NaOH), Polyvinylpyrrolidone (PVP) were purchased from China. All the materials were marked with the analytical grade and were used as received without any purification. The deionized (DI) water was used for the synthesis.

2.2. Synthesis of $(CeGdHfPrZr)O_2$ oxide nanoparticles

A simple hydrothermal synthesis was employed for the synthesis of high-entropy oxide nanoparticles. Initially, respective metal salts (0.001 M of each metal salt) were weighed and dissolved in 80 ml of DI water, followed by stirring at room temperature until all the salts were dissolved completely. Then PVP was added to the above transparent solution and stirred until the PVP dissolved completely. The molar ratio of PVP to metal salts is 1:2. Then, the required amount of NaOH solution was added dropwise until a pH of 10 was achieved, and stirring was continued for another 10 min. The reaction mixture was then transferred to a 100 ml hydrothermal reactor vessel and kept in a preheated oven at 80 °C for 6 h. After the completion of the reaction, the reactor vessel was cooled down to room temperature and washed with DI water multiple times until the pH of the solution was 7. The obtained precipitate was dried in an oven at 110 °C for 12 h to evaporate the solvent. The dried precipitate was ground in an agate mortar pestle, followed by air calcination in a muffle furnace at 500 °C for 4 h. The obtained **(**CeGdHfPrZr)O_2 powder was used for further characterization and photocatalytic investigation.

2.3. Characterization

The crystallinity of the prepared HEO was studied using XRD (Rigaku Ultima IV, Rigaku) using Cu-K_α radiation (λ = 1.54 Å) in the range of 20-80° with a scan speed of 1° per min. Rietveld refinement was done using the Fullprof program, and Williamson-Hall (W-H) analysis was done to assess the contribution of crystallite size and the lattice strain to XRD peak broadening. FESEM images were captured using a JEOL (JEOL JSM-7001F, JEOL) microscope operated at a potential of 20 kV. Similarly, the elemental quantification was done by energy-dispersive x-ray spectroscopy (EDS) equipped with a field emission scanning electron microscope (JEOL JSM-7001F, JEOL). The HRTEM image and SAED pattern were captured using a JEOL microscope (JEOL JEM-2100, JEOL) operated at an acceleration voltage of 175 kV. The optical properties were investigated using a UV-Visible

spectrophotometer (Shimadzu UV-2700) in both absorbance and reflectance modes. Fourier-transform infrared spectroscopy (FTIR) studies were performed on the powders using the Shimadzu IRAffinity-1S. Sample preparation for the FTIR studies involves the preparation of the pellet by mixing the powder photocatalyst and KBr (1:100 weight ratio). Data was collected in transmittance mode from 400-4000 cm^{-1}.

2.4. Photocatalytic degradation of Methylene Blue dye

The degradation of MB dye was performed in the presence of **(**CeGdHfPrZr)O_2 catalyst under UV light as an irradiation source. Initially, 50 mg of HEO catalyst was added to 100 ml of 20 mgL^{-1} MB solution, followed by the addition of 200 µl of H_2O_2 solution to boost the generation of hydroxyl radicals in the system. To initiate the adsorption-desorption equilibrium, the reaction solution was magnetically stirred for 60 min in the dark. After 60 min, the solution containing the catalyst and MB dye is irradiated with UV light (λ = 402 nm) which initiates the photocatalytic activity. Meanwhile, 3 mL of the reaction solution was taken out at a specific interval of time and centrifuged at a speed of 12000 rpm for 5 min to separate the catalyst from the reaction solution. The degradation of MB dye in the centrifuged solution was monitored using a UV-visible spectrophotometer from 400 nm to 800 nm. The solution containing MB dye was responsible for an absorption maximum of around 664 nm in the absorption spectra. Based on the intensity at 664 nm, the photocatalytic reaction kinetics were calculated. Several reaction parameters have been investigated, such as photocatalyst concentration (100, 250, 500, and 1000 mgL^{-1}), MB concentration (10, 25, 50, and 100 mgL^{-1}), and pH (2.5, 4.4, 8.6, and 10.5). In addition, control experiments have been carried out individually in the absence of a photocatalyst and irradiation source.

3. Results and discussions

The phase purity of calcined high-entropy **(**CeGdHfPrZr)O_2 oxide nanoparticles were examined by XRD. The X-ray diffraction pattern of the HEO oxide nanoparticle is shown in Fig. 1. All the reflections are indexed to the (111), (200), (220), (311), (222), (400), and (331) planes of the cubic fluorite structure. The obtained patterns are similar to those of pure CeO_2 oxide with ICDD card number: 01-073-6318 [41]. No additional reflections are observed in the calcined **(**CeGdHfPrZr)O_2 sample, which confirms the absence of other phases or impurities. As a result, the synthesized HEO is a single-phase material and has a cubic fluorite structure. The HEO exhibits a shift in the x-ray reflection at higher angles when compared with the standard pattern, indicating the emergence of a unique lattice parameter as a result of mixing five principal constituents.

To investigate further, Rietveld refinement was performed to fit the x-ray diffraction pattern to calculate the lattice parameter. The Rietveld refinement was fitted using a cubic fluorite structure using a space group Fm-3m (225) and the corresponding fit is displayed in Fig. 1b and the resulting fitting parameter is shown in Table S1. The Rietveld refinement fitting parameters indicate that the synthesized HEO is single phase, and the calculated lattice parameter is 5.331 Å. To estimate the crystallite size and lattice strain in the HEO oxide, the Williamson-Hall (W–H) method was employed (Fig. S2). Accordingly, an average crystallite size of 5.4 nm with a lattice strain of 1.78% is obtained. For HEO oxide systems, increased lattice strain results from the incorporation of different-sized metal cations into a single crystal structure. This increased lattice strain is one of the unique properties of a high-entropy oxide system (severe lattice distortion effect) [1].

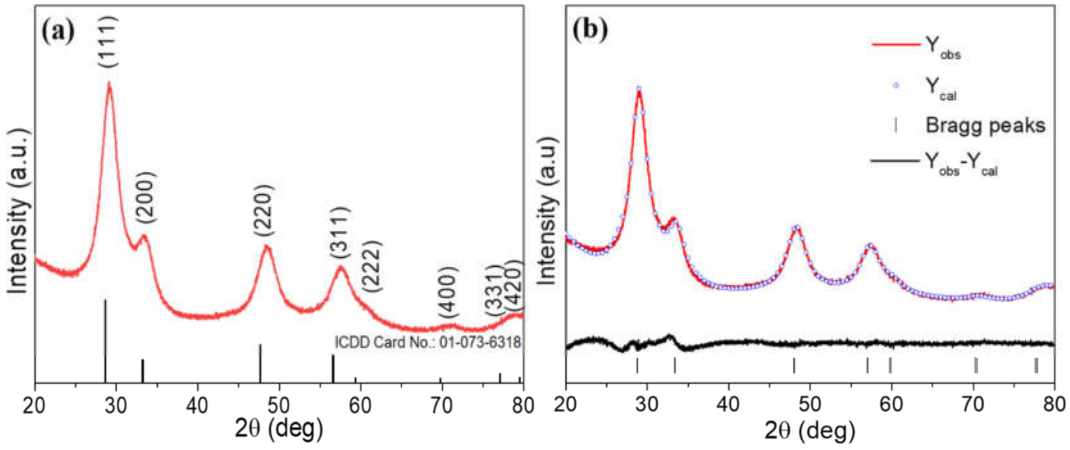

188

189 **Fig. 1.** (a) X-ray diffraction pattern of synthesized HEO oxide nanoparticles and (b) Rietveld
190 refinement fit of HEO.

191 To investigate the morphological features and elemental distribution of the synthesized
192 HEO oxide nanoparticles, FESEM was performed. Fig. 2(a) and (b) reveal agglomerated
193 spherical nanoparticles resulting from the hydrothermal synthesis route. In addition, to probe
194 the elemental distribution, elemental mapping was done and displayed in Fig. 2(c-i). It is
195 observed that all five principal elements are randomly distributed without any segregation. This
196 confirms the complete mixing of metal cations and their corresponding EDS spectra, as shown
197 in Fig. 2(j). As can be seen in Table S2, the chemical composition estimated from the EDS
198 spectrum of the HEO confirms that all five elements are present in nearly equimolar amounts.

spectral absorbance. This eventually decreases the bandgap of our synthesized HEO oxide nanoparticles. The indirect bandgap energies of HEO were calculated using the Kubelka-Munk (K-M) function, F(R) by plotting hν versus (F(R)∗ hν) (1/2) [7]. The band gap values were calculated by extrapolating the linear part of the graph (F(R)∗ hν) (1/2) = 0. Using this equation, a bandgap of 2.01 eV is obtained. The low bandgap value obtained for this **(**CeGdHfPrZr)O_2 composition is however important for photocatalytic applications as it will improve the spectral absorption in the visible region [46, 47] and the visual appearance of the HEO photocatalyst is shown in the inset of Fig. 4.

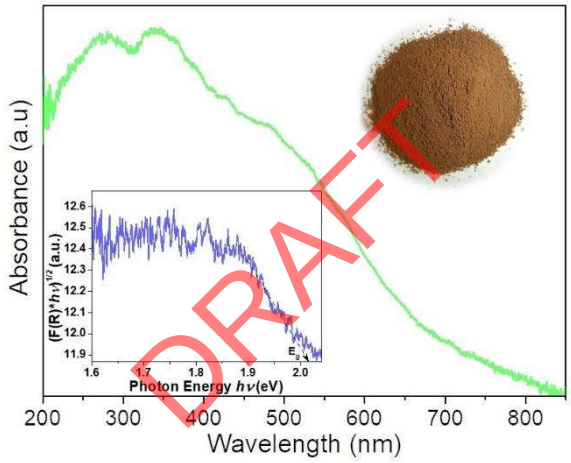

Fig. 4. UV-visible absorption spectrum of (CeGdHfPrZr)O_2 oxide powder and its physical appearance. Inset shows the bandgap calculation using the K-M function.

XPS was carried out to investigate the chemical environment of individual elements and is shown in fig.S2. Based on the wide energy survey spectrum, it was found that Ce3d, Gd4d, Hf4f, Zr3d, Pr3d, and O1s have characteristic peaks that corresponds to the existence of Ce, Gd, Hf, Zr, Pr, and O elements, respectively. The high-resolution Ce 3d XPS spectrum contains peaks at 885.28 eV, and 903.48 eV corresponding to Ce^{3+} while peaks at 882.28 eV, 888.28 eV, 898.19 eV, 900.58 eV, 907.38 eV, and 916.68 eV are attributed to Ce^{4+} species[48].

As a result, the synthesized photocatalyst contains defects in terms of oxygen vacancies, which is beneficial in photocatalytic investigations[6]. Similarly, two peaks whose binding energy located at 147.18 eV (Gd^{3+} $4d_{3/2}$) and 142.48 eV (Gd^{3+} $4d_{5/2}$) corresponds to Gd^{3+}. In case of Hf4f spectra, binding energies at 17.08 eV, 18.58 eV correspond to the spin orbit doublets Hf $4f_{7/2}$, and Hf $4f_{5/2}$[49]. The Pr3d spectrum contain two peaks having binding energies 928.18 eV and 932.28 eV indicating the presence of Pr^{3+} and Pr^{4+} respectively[50]. The binding energies at 181.58 eV and 183.78 eV correspond to doublet Zr $3d_{5/2}$–Zr $3d_{3/2}$ which is due to the presence of Zr^{4+}[51]. The oxygen spectra contains three peaks at 532.58 eV, 531.08 eV, 529.18 eV denoting hydroxyl groups, adsorbed oxygen, and lattice oxygen[52]. Therefore, based on the XPS studies, it is evident that $(CeGdHfPrZr)O_2$ high-entropy oxide contains oxygen vacancies enabling faster photocatalytic performances.

3.1 Photocatalytic degradation of methylene blue dye

To test the photocatalytic activity of synthesized HEO, a standard methylene blue dye is used as a model industrial dye, and UV light is used as an irradiation source. A well-known pollutant, methylene blue, is used in a variety of industries for a variety of purposes. In order to eradicate such hazardous pollutants from water bodies, it is vital to develop advanced oxidation strategies by designing novel photocatalysts. Here, HEO is investigated as a novel photocatalyst for MB degradation.

3.1.1 Effect of catalyst loading

To investigate the effect of catalyst loading on the photocatalytic property, different concentrations of HEO catalyst, such as 100 mg/L, 250 mg/L, 500 mg/L, and 1000 mg/L were added to the 20 mg/L MB solution, and its photocatalytic studies were monitored using a UV-visible spectrophotometer, as displayed in Fig. S3. The absorbance spectra revealed the characteristic absorption peak of MB, which is located at 664 nm and the visual observation is

seen in Fig. 5(a). After 60 min of stirring in the dark, the intensity of the MB decreases slightly, which confirms the adsorption of MB dye molecules on the surface of the photocatalyst. After the UV light is switched ON, the intensity at 664 nm of MB decreases with time, indicating the process of degradation of the dye molecule. The colour of the MB solution lightens with increasing irradiation time and can be visually observed, as shown in Fig. 5(a). The C/C_0 plot displayed in Fig. 5(b) shows the variation in MB degradation with different catalyst concentrations. It is observed that with an increase in catalyst concentration, the kinetics of MB degradation increased. This is attributed to an increase in the number of active sites, which is responsible for the generation of electron-hole pairs, generating more radicals, and improving the degradation of MB dye. However, a maximum MB degradation is achieved for a catalyst loading of 500 mg/L above which the MB degradation is slowed down. This is attributed to the blocking of UV light into the MB dye solution by the catalyst, resulting in the saturation of available photons and thus limiting the production of electron-hole pairs.

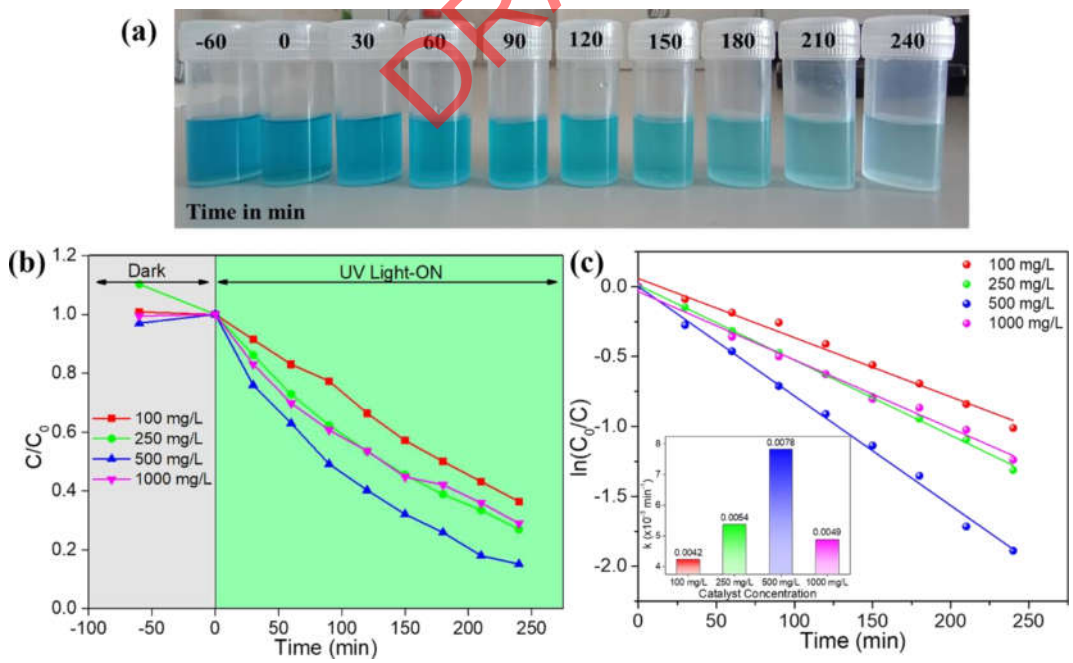

Fig. 5. (a) Visual appearance of MB dye solution at various time intervals in the presence of $(CeGdHfPrZr)O_2$ photocatalyst under UV irradiation. (b) A plot of C/C_0 of MB degradation

for various concentrations of the catalyst under UV irradiation and (c) its corresponding $\ln(C_0/C)$ plot (inset: rate constant).

Control experiments were also carried out to outline the importance of the catalyst and UV-light source individually. Fig. S4 shows the absorption spectra of the MB dye solution in the absence of a photocatalyst (Fig. S4(a)) and UV source (Fig. S4(b)). It is evident that in the absence of any one, the MB degradation is not favorable, meaning both the UV light source and photocatalyst are necessary for the photocatalytic reaction to carry on.

In general, the photocatalytic degradation of MB follows pseudo-first-order kinetics, which is monitored by using a UV-visible spectrophotometer[53, 54]. Let $[MB]_t$ be the concentration of MB at time 't' and $[MB]_0$ is the concentration of MB at time zero. Therefore, the rate of the degradation reaction depends on $[MB]_t$. The rate constant k of the reaction is given by $k * t = \ln\left(\frac{[MB]_0}{[MB]_t}\right)$. The calculated rate constants are 0.0042, 0.0054, 0.0078, and 0.0049 min^{-1} respectively for 100 mg/L, 250 mg/L, 500 mg/L, and 1000 mg/L catalysts. In a system with a photocatalyst loading of 500 mg/L, a maximum rate constant of 0.0078 min^{-1} is calculated, while a minimum value of 0.0042 min^{-1} is obtained for a system with a 100 mg/L catalyst loading. This being the case, we used a catalyst loading of 500 mg/L for further investigations.

3.1.2 Effect of methylene blue concentration

Secondly, the effect of MB dye concentration was evaluated to study the impact of MB on photocatalytic reaction kinetics. The concentration of dyes in wastewater discharge varies and are industry-dependent that are releasing the dyes. Therefore, it is necessary to study the potential of photocatalysts on the impact of initial dye concentration. Moreover, the rate of degradation is determined by the probability of hydroxyl radical formation on the catalyst surface and the reaction of dye molecules with the hydroxyl radical. In this regard, several

initial dye concentrations such as 10 mg/L, 25 mg/L, 50 mg/L, and 100 mg/L were used, and the photocatalytic degradation studies have been evaluated as shown in Fig. 6(a) and (b) and Fig. S5. For lower MB concentrations, the degradation is faster, with a rate constant of 0.0093 min^{-1}. This is probably due to the availability or generation of excess/sufficient hydroxyl radicals by the photocatalyst, which increases the degradation kinetics of MB dye.

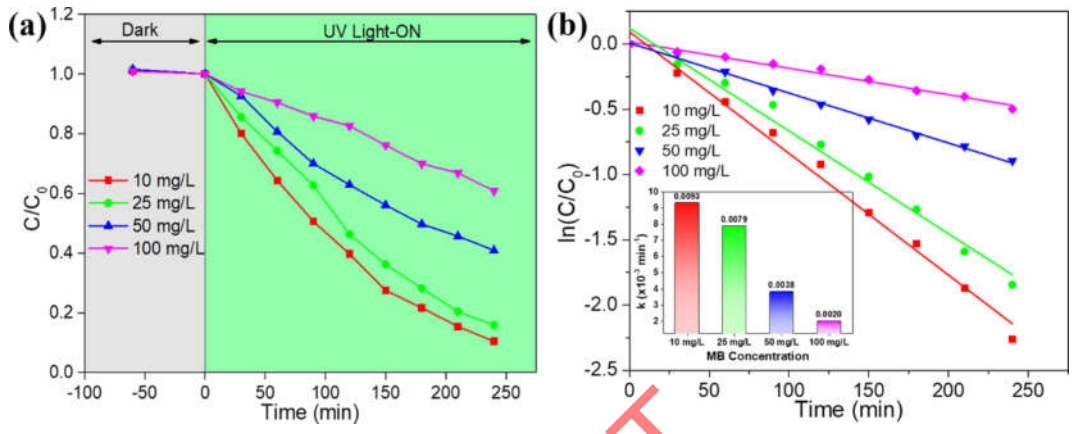

Fig. 6. Effect of MB dye concentration on the photocatalytic reaction (a) Plot of C/C_0 of MB degradation under UV-light irradiation and (b) its corresponding $ln(C_0/C)$ plot (inset: rate constant). (Catalyst: 500 mg/L)

With an increase in MB concentration, the rate constant declines consistently, and a value of 0.002 min^{-1} is obtained for an MB concentration of 100 mg/L. Despite the fact that the rate constant appears to decrease with increasing MB concentration, the quantity of MB dye degraded in all cases is 0.0093 mg L^{-1} min^{-1}, 0.1975 mg L^{-1} min^{-1}, 0.19 mg L^{-1} min^{-1}, and 0.2 mg L^{-1} min^{-1} respectively for 10 mg/L, 25 mg/L, 50 mg/L, and 100 mg/L of dye concentration. The observed values seems intriguing since the amount of MB dye degraded is the same in all cases except for the samples that contain10 mg/L of MB dye. Similar results have been observed in other reported literature [55]. One probable explanation is the effect of intermediary products on MB dye degradation. The intermediate products compete with MB dye for hydroxyl radicals[56]. A higher concentration of MB dye molecules around the active

sites of photocatalyst inhibited light penetration to the surface of the catalyst as a result of the dye molecules. However, the explanation is not completely understood, so further research is necessary to get a better understanding of the scientific rationale for the observed results.

3.1.3 Effect of pH

As discussed in the earlier section, similar to the MB concentration, the pH of industrial water discharge is uncertain, and it is important to investigate the effect of solution pH on the photocatalytic degradation of MB dye. MB adsorption on photocatalysts is influenced by the pH value since it depends on the surface state of the photocatalyst. The surface charge of the catalyst is altered by pH values, which may either have a positive or negative impact on MB degradation kinetics. Therefore, using 0.1 mol L^{-1} HCl or 0.1 mol L^{-1} NaOH, the pH of the photocatalytic reaction mixture was varied, and its respective C/C_0 and rate constant plots are displayed in Fig. 7 (a), (b) and Fig. S6.

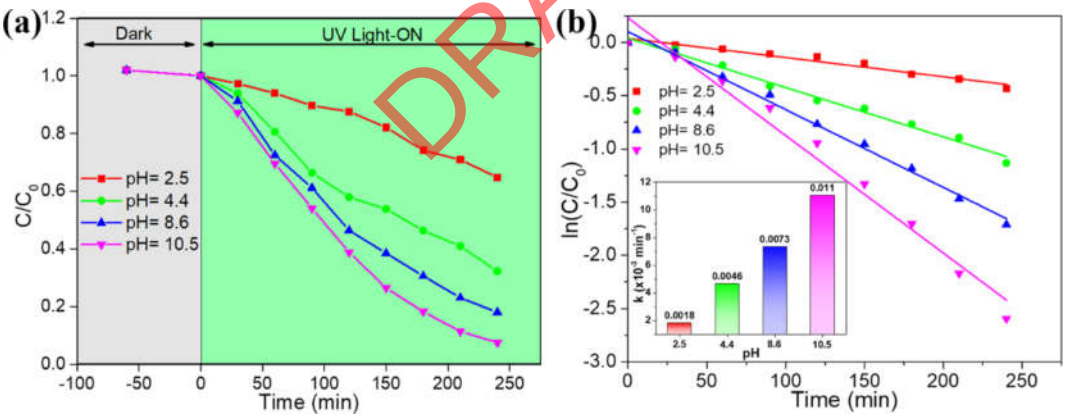

Fig. 7. Effect of pH on the photocatalytic degradation of MB dye solution (a) Plot of C/C_0 of MB degradation for various concentrations of the catalyst under UV irradiation and (b) its corresponding $\ln(C_0/C)$ plot (inset: rate constant). (Catalyst: 500 mg/L; MB: 20 mg/L)

It is observed that the photocatalyst underperformed at acidic pH values, with the lowest rate constant value of 0.0018 min^{-1} (pH = 2.5). For a pH value of 4.4, a rate constant of 0.046 min^{-1} is obtained. In contrast, at alkaline pH, increased photocatalytic degradation of MB dye

is observed. The faster reaction kinetics resulted in a rate constant of 0.011 min^{-1} for a pH of 10.5 while a rate constant of 0.0073 min^{-1} was obtained for a reaction pH of 8.6. The reason for improved photodegradation of MB dye in alkaline conditions is due to the surface charges present on the catalyst surface. In a basic pH environment, the photocatalyst surface is negatively charged due to the presence of larger quantities of OH^- ions. Similarly, under acidic conditions, the nanoparticle is positively charged. As a result, the negatively charged photocatalyst surface improves the adsorption of the cationic MB dye, increasing the photodegradation kinetics [57]. Another possible reason for improved photodegradation of MB dye at a basic pH is owing to the generation of hydroxyl radicals in the alkaline environment. There is a presence of an excess of OH^- in the alkaline solution. On exposure to UV-light irradiation, holes that are formed on the photocatalyst surface create hydroxyl radicals by the photooxidation of OH^- [58]. This generated hydroxyl radical is expected to be the main oxidizing species involved in the degradation of MB dye.

3.1.4 Mechanism of MB dye degradation

To understand the mechanism of MB dye degradation by the HEO catalyst, it is necessary to determine the band positions of the photocatalyst from the UV-visible absorption spectrum. The band positions play a crucial role in determining the performance of the photocatalyst [6]. With the help of Mulliken electronegativity, the valence band (E_{VB}) and conduction band (E_{CB}) potentials can be calculated using the following equations (1) and (2)

$$E_{CB} = \chi - E^e - 0.5\,E_g \quad (1)$$

$$E_{VB} = E_{CB} + E_g \quad (2)$$

where E^e is the energy of free electrons on the hydrogen scale (4.5 eV), E_g corresponds to the bandgap of the material, which can be estimated from the Tauc plot (2.01 eV in this case) and

χ denotes the electronegativity of oxides. Accordingly, equation (3) is used to calculate the electronegativity of the overall semiconductor oxide[6].

$$\chi = (\chi A^a \chi B^b \chi C^c \chi D^d \chi E^e \chi F^f)^{1/(a+b+c+d+e+f)} \quad (3)$$

where a, b, c, d, e, and f are the number of atoms present in the compound, while A, B, C, D, E, and F are the five metal cations and one anion present in the system. The electronegativity of an individual atom can be found using (4)

$$\chi A = \frac{1}{2}(E_{EA}A + E_{IE}A) \quad (4)$$

where E_{EA} and E_{IE} are electron affinity energy and ionization energy, respectively.

Using the equations (1), (2), (3), and (4), the value of E_{VB} and E_{CB} is estimated to be +2.101 eV and +0.091 eV versus a normal hydrogen electrode (NHE), respectively.

Fig. 8 shows the possible mechanism for the degradation of MB dye by HEO photocatalyst. On exposure to UV light over the photocatalytic reaction solution containing MB dye, HEO photocatalyst, and H_2O_2, electron-hole pairs are generated on the surface of the photocatalyst, as displayed in equation (5). The electrons stay in the conduction band while the holes stay in the valance band. Next, the holes in the valance band react with adsorbed water and hydroxyl ions to produce $^{\bullet}OH$ radicals, as in equations (6) and (7). This reaction pathway is possible because the calculated E_{VB} of the photocatalyst (+2.101 eV) is higher than that of the redox potential of $^{\bullet}OH/OH^-$ (+1.89 eV) [59].

$$h\upsilon + HEO\ photocatalyst \longrightarrow e_{CB}^- + h_{VB}^+ \quad (5)$$

$$H_2O + h_{VB}^+ \longrightarrow {}^{\bullet}OH + H^+ \quad (6)$$

$$OH^- + h_{VB}^+ \longrightarrow {}^{\bullet}OH \quad (7)$$

$$e_{CB}^- + H_2O_2 \longrightarrow + {}^{\bullet}OH + OH^- \quad (8)$$

$$^{\bullet}OH + MB\ dye \longrightarrow Degradation\ product \quad (9)$$

Additional hydroxyl radicals are generated in the presence of H_2O_2 by reacting with the conduction band electrons, as indicated in equation (8). It should be noted that the generation of superoxide radicals ($^{\bullet}O_2^-$) is inhibited in the current system due to the lower E_{CB} values of the HEO catalyst. The redox potential of $O_2/\ ^{\bullet}O_2^-$ is -0.33 eV while the calculated E_{CB} of the photocatalyst is +0.091 eV which is much lower than what is necessary for the reduction of O_2. Therefore, the generated free radicals ($^{\bullet}OH$) interact with the MB dye, and the demethylation process occurs by breaking the N-CH_3 bond (equation (9)). A scavenging experiment was conducted with iso-propyl alcohol in order to confirm the involvement of hydroxyl radicals in the degradation of MB dye [60]. Based on the scavenging results (Fig. 8(b)), it appears that MB is marginally degraded in the absence of hydroxyl radicals. Therefore, the hydroxyl radical is the main reactive species involved in the photodegradation of MB dye. Finally, the MB dye is degraded into H_2O, CO_2, ammonium ions, and sulfate ions [61].

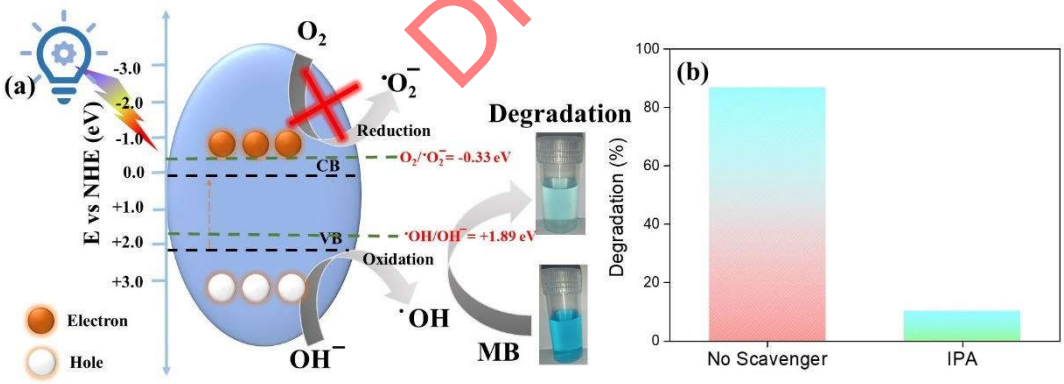

Fig. 8. (a) Schematic displaying the mechanism of photocatalytic degradation of MB dye using high-entropy $(CeGdHfPrZr)O_2$ oxide photocatalyst and (b) radical scavenging experiment on the photocatalytic degradation of MB dye solution .

To further investigate photocatalyst stability, recycling reactions were carried out for the degradation of MB dye using the HEO catalyst. After the end of each cycle, the catalyst

was separated by centrifuge and washed with DI water, followed by drying at 80 °C and being reused for the subsequent cycle. The degradation kinetics of MB decolorization during five consecutive cycles under UV-light irradiation are displayed in Fig. 9(a) and its rate constant plots are depicted in Fig. 9(b).

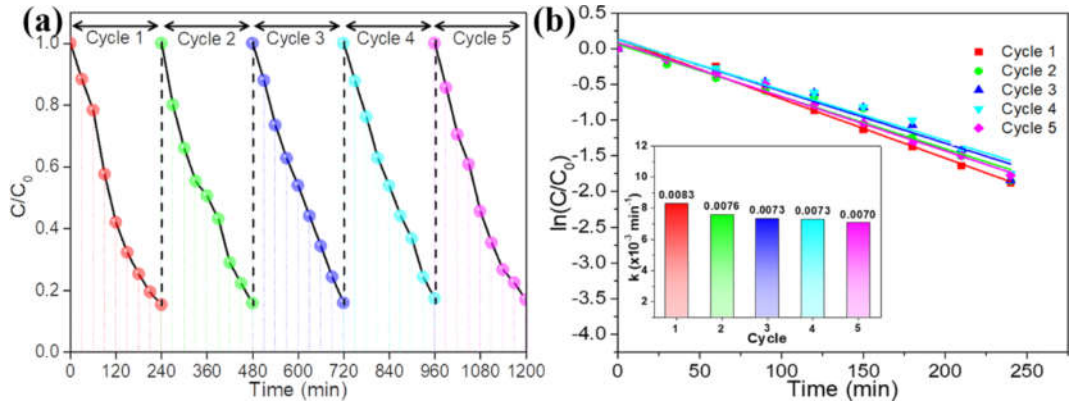

Fig. 9. (a) Recyclability test for the photocatalytic degradation of MB dye solution using $(CeGdHfPrZr)O_2$ catalyst under UV-light irradiation and (b) its corresponding $\ln(C_0/C)$ plot (inset: rate constant). (Catalyst: 500 mg/L; MB: 20 mg/L)

According to the results, the photocatalytic activity of the HEO catalyst was stable over the course of five cycles. The rate constant of MB decolorization decreased slightly from 0.0083 to 0.0070 min^{-1}, indicating that the HEO catalyst had good stability. To probe the structural properties of the HEO catalyst, XRD was performed on the recycled photocatalyst after 5 cycles, and the X-ray pattern is displayed in Fig. S7. The XRD results confirm the stability of the catalyst without displaying any structural transformation during the photocatalytic studies. In addition, FTIR spectroscopy has been carried out to investigate the surface functional groups present on the surface of the recycled photocatalyst, and the plot is displayed in Fig. S8. By comparing the FTIR spectra of the photocatalyst before and after MB degradation, it is clear that the catalyst has retained its structure and there has been no significant change in the functional groups present in the catalyst. As a result, it is evident that

the synthesized high-entropy oxide catalyst exhibits high stability and is capable of being recycled numerous times without losing any photocatalytic activity.

4. Conclusion

A simple hydrothermal synthesis route was used to synthesize high-entropy (CeGdHfPrZr)O_2 oxide nanoparticles. The synthesized HEO exhibits a single-phase cubic fluorite crystal structure with a mean crystallite size of 5.4 nm. A higher lattice strain is found in the HEO system due to the presence of different-sized metal cations. The MB degradation kinetics were evaluated by varying the concentration of the photocatalyst, MB dye, and pH. MB degradation studies indicate better photocatalytic activity by the synthesized HEO photocatalysts. Moreover, the degradation kinetics are dependent on several experimental conditions, such as catalyst concentration, dye concentration, and solution pH. Poor MB dye degradation kinetics are observed at higher photocatalyst concentrations, which limits photon penetration into the reaction solution. The photocatalyst performed better at a basic pH as a result of excess hydroxyl radical generation, improving MB dye degradation. Moreover, based on the calculated E_{VB} and E_{CB} values, hydroxyl radicals are responsible for the degradation of MB dye, which is confirmed by the hydroxyl radical scavenging study. In addition, the HEO catalyst material was found to be stable and reused for several degradation cycles without decreasing the efficiency of the photocatalyst. (CeGdHfPrZr)O_2 was found to be a promising photocatalyst for the degradation of organic pollutants under UV irradiation. The use of novel high-entropy oxides in water treatment applications is an attractive one.

CRediT authorship contribution statement

Mariappan Anandkumar: Conceptualization, Data curation, Formal analysis, Investigation, Methodology, Validation, Writing – original draft, Writing – review & editing, Visualization. **Kannan P.K.:** Data curation, Formal analysis, Investigation, Validation, Writing – review &

editing. **Shanmugavel Sudarsan:** Investigation, Writing - Review & Editing. **Evgeny Trofimov:** Conceptualization, Funding acquisition, Project administration, Supervision

Declaration of Competing Interest

There are no conflicts to declare.

Acknowledgements

The study was supported by the Russian Science Foundation Grant No. 22-23-00243, https://rscf.ru/project/22-23-00243/

References:

[1] M. Anandkumar, E. Trofimov, Synthesis, Properties, and Applications of High-Entropy Oxide Ceramics: Current Progress and Future Perspectives, Journal of Alloys and Compounds, (2023) 170690.

[2] S. Akrami, P. Edalati, M. Fuji, K. Edalati, High-entropy ceramics: Review of principles, production and applications, Materials Science and Engineering: R: Reports, 146 (2021) 100644.

[3] S.H. Albedwawi, A. AlJaberi, G.N. Haidemenopoulos, K. Polychronopoulou, High entropy oxides-exploring a paradigm of promising catalysts: A review, Materials & Design, 202 (2021) 109534.

[4] X. Liu, P. Zhang, Y. Han, W. Pan, C. Wan, Tailoring thermal and mechanical properties of rare earth niobates by coupling entropy and composite engineering, Journal of the European Ceramic Society, 43 (2023) 1141-1146.

[5] Z. Lou, P. Zhang, J. Zhu, L. Gong, J. Xu, Q. Chen, M.J. Reece, H. Yan, F. Gao, A novel high-entropy perovskite ceramics $Sr_{0.9}La_{0.1}(Zr_{0.25}Sn_{0.25}Ti_{0.25}Hf_{0.25})O_3$ with low thermal conductivity and high Seebeck coefficient, Journal of the European Ceramic Society, 42 (2022) 3480-3488.

[6] M. Anandkumar, A. Lathe, A.M. Palve, A.S. Deshpande, Single-phase $Gd_{0.2}La_{0.2}Ce_{0.2}Hf_{0.2}Zr_{0.2}O_2$ and $Gd_{0.2}La_{0.2}Y_{0.2}Hf_{0.2}Zr_{0.2}O_2$ nanoparticles as efficient photocatalysts for the reduction of Cr(VI) and degradation of methylene blue dye, Journal of Alloys and Compounds, 850 (2021) 156716.

[7] M. Anandkumar, P.M. Bagul, A.S. Deshpande, Structural and luminescent properties of Eu^{3+} doped multi-principal component $Ce_{0.2}Gd_{0.2}Hf_{0.2}La_{0.2}Zr_{0.2}O_2$ nanoparticles, Journal of Alloys and Compounds, 838 (2020) 155595.

[8] C. Zhou, X. Zhang, S. Li, J. Yan, X. Qi, Dielectric and energy storage properties of $(La,Li)_x[(Bi,Na)BaSrCa]_{1-x}TiO_3$ high-entropy perovskite ceramics, Ceramics International, 48 (2022) 24268-24275.

[9] W. Xiong, H. Zhang, Z. Hu, M.J. Reece, H. Yan, Low thermal conductivity in A-site high entropy perovskite relaxor ferroelectric, Applied Physics Letters, 121 (2022) 112901.

[10] A. Kumar, D. Dragoe, D. Berardan, N. Dragoe, Thermoelectric properties of high-entropy rare-earth cobaltates, Journal of Materiomics, 9 (2023) 191-196.

[11] G.H.J. Johnstone, M.U. González-Rivas, K.M. Taddei, R. Sutarto, G.A. Sawatzky, R.J. Green, M. Oudah, A.M. Hallas, Entropy Engineering and Tunable Magnetic Order in the Spinel High-Entropy Oxide, Journal of the American Chemical Society, 144 (2022) 20590-20600.

[12] H. Minouei, M. Jalaly, M. Kheradmandfard, M. Saboktakin Rizi, D.-E. Kim, S.I. Hong, Rapid microwave-assisted synthesis and magnetic properties of high-entropy spinel $(Cr_{0.2}Mn_{0.2}Fe_{0.2}Co_{0.2-x}Ni_{0.2}Zn_x)_3O_4$ nanoparticles, Ceramics International, 49 (2023) 11885-11892.

[13] S. Mallesh, J.-S. Noh, Y.-W. Nam, Structure and magnetic properties of $(Mg_{1/6}Zn_{1/6}Mn_{1/6}Co_{1/6}Ni_{1/6}Fe_{1/6})_3O_4$ nanocrystalline high-entropy oxide synthesized using a sol-gel auto combustion approach, Journal of Magnetism and Magnetic Materials, 564 (2022) 170108.

[14] S. Akrami, Y. Murakami, M. Watanabe, T. Ishihara, M. Arita, M. Fuji, K. Edalati, Defective high-entropy oxide photocatalyst with high activity for CO_2 conversion, Applied Catalysis B: Environmental, 303 (2022) 120896.

[15] Z. Liu, Z. Tang, Y. Song, G. Yang, W. Qian, M. Yang, Y. Zhu, R. Ran, W. Wang, W. Zhou, Z. Shao, High-Entropy Perovskite Oxide: A New Opportunity for Developing Highly Active and Durable Air Electrode for Reversible Protonic Ceramic Electrochemical Cells, Nano-Micro Letters, 14 (2022) 217.

[16] Z.-w. Li, Z.-h. Chen, J.-j. Xu, Enhanced energy storage performance of $BaTi_{0.97}Ca_{0.03}O_{2.97}$-based ceramics by doping high-entropy perovskite oxide, Journal of Alloys and Compounds, 922 (2022) 166179.

[17] V.R. Naganaboina, S. Bonam, M. Anandkumar, A.S. Deshpande, S.G. Singh, Humidity-Independent Methane Gas Detection in $Gd_{0.2}La_{0.2}Ce_{0.2}Hf_{0.2}Zr_{0.2}O_2$-Based Sensor Using Polynomial Regression Analysis, IEEE Electron Device Letters, 43 (2022) 2153-2156.

[18] V.R. Naganaboina, M. Anandkumar, A.S. Deshpande, S.G. Singh, Single-Phase High-Entropy Oxide Nanoparticles for Wide Dynamic Range Detection of CO_2, ACS Applied Nano Materials, 5 (2022) 4524-4536.

[19] V.R. Naganaboina, M. Anandkumar, A.S. Deshpande, S.G. Singh, Single-phase high-entropy oxide-based chemiresistor: Toward selective and sensitive detection of methane gas for real-time applications, Sensors and Actuators B: Chemical, 357 (2022) 131426.

[20] K. Ren, Q. Wang, G. Shao, X. Zhao, Y. Wang, Multicomponent high-entropy zirconates with comprehensive properties for advanced thermal barrier coating, Scripta Materialia, 178 (2020) 382-386.

[21] S.K. Shaw, P. Kumari, A. Sharma, N. Jatav, A. Gangwar, N.S. Anuraag, P. Rajput, S. Kavita, S.S. Meena, M. Vasundhara, I. Sinha, N.K. Prasad, Assessment of ionic site

distributions in magnetic high entropy oxide of $(Mn_{0.2}Fe_{0.2}Co_{0.2}Ni_{0.2}Zr_{0.2})_3O_4$ and its catalytic behaviour, Physica B: Condensed Matter, 652 (2023) 414653.

[22] L. Danyang, S. Liping, L. Qiang, X. Tian, H. Lihua, Z. Hui, High-entropy oxide $(Fe_{0.2}Zn_{0.2}Co_{0.2}Ni_{0.2}Cu_{0.2})Fe_2O_4$: An efficient and stable spinel-type electrocatalyst for H_2O_2 production in alkaline media, Journal of Alloys and Compounds, 913 (2022) 165148.

[23] Y. Hu, M. Anandkumar, J. Joardar, X. Wang, A.S. Deshpande, K.M. Reddy, Effective band gap engineering in multi-principal oxides (CeGdLa-Zr/Hf)Ox by temperature-induced oxygen vacancies, Scientific Reports, 13 (2023) 2362.

[24] P. Edalati, Y. Itagoe, H. Ishihara, T. Ishihara, H. Emami, M. Arita, M. Fuji, K. Edalati, Visible-light photocatalytic oxygen production on a high-entropy oxide by multiple-heterojunction introduction, Journal of Photochemistry and Photobiology A: Chemistry, 433 (2022) 114167.

[25] Y. Yu, S. Liu, H. Wang, S. Zhang, N. Wang, W. Jiang, C. Liu, W. Ding, Z. Zhang, C. Dong, Design, synthesis and photocatalytic performance of $A_{32}Ti_8Sn_8Nb_4Ta_4Me_8O_{96}$ (A=Ba, Sr; Me=Fe, Ga) perovskite structure high entropy oxides, Journal of Solid State Chemistry, 317 (2023) 123694.

[26] A.M. Elgarahy, K.Z. Elwakeel, S.H. Mohammad, G.A. Elshoubaky, A critical review of biosorption of dyes, heavy metals and metalloids from wastewater as an efficient and green process, Cleaner Engineering and Technology, 4 (2021) 100209.

[27] R. Al-Tohamy, S.S. Ali, F. Li, K.M. Okasha, Y.A.G. Mahmoud, T. Elsamahy, H. Jiao, Y. Fu, J. Sun, A critical review on the treatment of dye-containing wastewater: Ecotoxicological and health concerns of textile dyes and possible remediation approaches for environmental safety, Ecotoxicology and Environmental Safety, 231 (2022) 113160.

[28] Z. Zhang, X. Dong, Y. Wang, N. Zheng, H. Ma, X. Zhang, Co_9S_8/CdS heterostructures as efficient photocatalysts for degradation of organic pollutant, Ceramics International, 49 (2023) 25207-25215.

[29] D.C. Onwudiwe, V.M. Nkwe, O.C. Olatunde, H. Ferjani, Graphitic carbon nitride functionalized with Cu-doped Bi_2S_3 as a heterostructure photocatalyst for the visible light degradation of methyl orange, Ceramics International, 49 (2023) 19451-19462.

[30] A. Saravanan, V.C. Deivayanai, P.S. Kumar, G. Rangasamy, R.V. Hemavathy, T. Harshana, N. Gayathri, K. Alagumalai, A detailed review on advanced oxidation process in treatment of wastewater: Mechanism, challenges and future outlook, Chemosphere, 308 (2022) 136524.

[31] A.D. Gupta, H. Singh, S. Varjani, M.K. Awasthi, B.S. Giri, A. Pandey, A critical review on biochar-based catalysts for the abatement of toxic pollutants from water via advanced oxidation processes (AOPs), Science of The Total Environment, 849 (2022) 157831.

[32] R.-G. Ciocarlan, E.M. Seftel, R. Gavrila, M. Suchea, M. Batuk, M. Mertens, J. Hadermann, P. Cool, Spinel nanoparticles on stick-like Freudenbergite nanocomposites as effective smart-removal photocatalysts for the degradation of organic pollutants under visible light, Journal of Alloys and Compounds, 820 (2020) 153403.

[33] S. Sudarsan, M. Anandkumar, E.A. Trofimov, Synthesis and characterization of copper ferrite nanocomposite from discarded printed circuit boards as an effective photocatalyst for Congo red dye degradation, Journal of Industrial and Engineering Chemistry, 131 (2024) 208-220.

[34] S. Zhong, P. Wang, Y. Chen, Y. Wang, M. Lin, C. Lin, T. Lin, M. Gao, C. Zhao, J. Lin, X. Wu, A facile method for access to high efficient piezo-photocatalytic synergy of $Ba_{0.85}Sr_{0.15}TiO_3$ through tuning grain size, Curie temperature and energy band gap, Journal of Alloys and Compounds, 967 (2023) 171710.

572 [35] M. Umar, H. Ajaz, M. Javed, S. Mansoor, S. Iqbal, A. Alhujaily, A. Bahadur, R.A.
573 Althobiti, E. Alzahrani, A.-E. Farouk, F.F. Al-Fawzan, E.B. Elkaeed, Designing of Te-doped
574 ZnO and S-g-C_3N_4 /Te-ZnO nano-composites as excellent photocatalytic and antimicrobial
575 agents, Polyhedron, 245 (2023) 116664.
576 [36] A. Bahadur, S. Iqbal, M. Javed, S.S. Hassan, S. Nadeem, A. Akbar, R.M. Alzhrani, M.M.
577 Al-Anazy, E.B. Elkaeed, N.S. Awwad, H.A. Ibrahium, A. Mohyuddin, Construction of a binary
578 S-scheme S-g-C_3N_4/Co-ZF heterojunction with enhanced spatial charge separation for
579 sunlight-driven photocatalytic performance, RSC Advances, 12 (2022) 23263-23273.
580 [37] K. Aroosh, M. Javed, N. Hussain, A. Alhujaily, S. Iqbal, M.T. Alotaibi, M. Faizan, M.S.
581 Khan, A. Bahadur, M.A. Qayyum, N.S. Awwad, Y. Jazaa, F.F. Al-Fawzan, E.B. Elkaeed,
582 Construction of Te-ZnO@S-g-C_3N_4 Heterojunction Nanocomposites for the Efficient Removal
583 of Methylene Blue, Antifungal Activity, and Adsorption of Cr(VI) Ion, Adsorption Science &
584 Technology, 2023 (2023) 6736182.
585 [38] M. Anandkumar, P.K. Kannan, S. Sudarsan, D.A. Uchaev, E.A. Trofimov, Reusable high-
586 entropy oxide environmental photocatalyst towards toxic Cr(VI) reduction with tailored
587 bandgap via solution combustion synthesis, Advanced Powder Technology, 35 (2024) 104429.
588 [39] M.F. Lanjwani, M. Tuzen, M.Y. Khuhawar, T.A. Saleh, Trends in photocatalytic
589 degradation of organic dye pollutants using nanoparticles: A review, Inorganic Chemistry
590 Communications, 159 (2024) 111613.
591 [40] K. Kannan, D. Radhika, D. Gnanasangeetha, L.S. Krishna, K. Gurushankar, Y^{3+} and Sm^{3+}
592 co-doped mixed metal oxide nanocomposite: Structural, electrochemical, photocatalytic, and
593 antibacterial properties, Applied Surface Science Advances, 4 (2021) 100085.
594 [41] M. Anandkumar, S. Bhattacharya, A.S. Deshpande, Low temperature synthesis and
595 characterization of single phase multi-component fluorite oxide nanoparticle sols, RSC
596 Advances, 9 (2019) 26825-26830.

[42] D.N. Durgasri, T. Vinodkumar, P. Sudarsanam, B.M. Reddy, Nanosized CeO_2–Gd_2O_3 Mixed Oxides: Study of Structural Characterization and Catalytic CO Oxidation Activity, Catalysis Letters, 144 (2014) 971-979.

[43] M. Anandkumar, G. Vinothkumar, K. Suresh Babu, Synergistic effect of gold supported on redox active cerium oxide nanoparticles for the catalytic hydrogenation of 4-nitrophenol, New Journal of Chemistry, 41 (2017) 6720-6729.

[44] M. Guo, J. Lu, Y. Wu, Y. Wang, M. Luo, UV and Visible Raman Studies of Oxygen Vacancies in Rare-Earth-Doped Ceria, Langmuir, 27 (2011) 3872-3877.

[45] M. Anandkumar, C.H. Ramamurthy, C. Thirunavukkarasu, K.S. Babu, Influence of age on the free-radical scavenging ability of CeO_2 and Au/CeO_2 nanoparticles, Journal of Materials Science, 50 (2015) 2522-2531.

[46] K. Nagaveni, M.S. Hegde, N. Ravishankar, G.N. Subbanna, G. Madras, Synthesis and Structure of Nanocrystalline TiO_2 with Lower Band Gap Showing High Photocatalytic Activity, Langmuir, 20 (2004) 2900-2907.

[47] M. Mishra, D.-M. Chun, α-Fe_2O_3 as a photocatalytic material: A review, Applied Catalysis A: General, 498 (2015) 126-141.

[48] F. Meng, C. Zhang, Z. Fan, J. Gong, A. Li, Z. Ding, H. Tang, M. Zhang, G. Wu, Hydrothermal synthesis of hexagonal CeO_2 nanosheets and their room temperature ferromagnetism, Journal of Alloys and Compounds, 647 (2015) 1013-1021.

[49] F. Ambriz-Vargas, G. Kolhatkar, R. Thomas, R. Nouar, A. Sarkissian, C. Gomez-Yáñez, M.A. Gauthier, A. Ruediger, Tunneling electroresistance effect in a Pt/$Hf_{0.5}Zr_{0.5}O_2$/Pt structure, Applied Physics Letters, 110 (2017).

[50] W. Zhang, M. Shiraiwa, N. Wang, T. Ma, K. Fujii, E. Niwa, M. Yashima, Pr/Ba cation-disordered perovskite $Pr_{2/3}Ba_{1/3}CoO_{3-\delta}$ as a new bifunctional electrocatalyst for oxygen

621 reduction and oxygen evolution reactions, Journal of the Ceramic Society of Japan, 126 (2018)
622 814-819.
623 [51] O.A. Bulavchenko, Z.S. Vinokurov, T.N. Afonasenko, P.G. Tsyrul'nikov, S.V. Tsybulya,
624 A.A. Saraev, V.V. Kaichev, Reduction of mixed Mn–Zr oxides: in situ XPS and XRD studies,
625 Dalton Transactions, 44 (2015) 15499-15507.
626 [52] G. Wang, Q. Mu, T. Chen, Y. Wang, Synthesis, characterization and photoluminescence
627 of CeO_2 nanoparticles by a facile method at room temperature, Journal of Alloys and
628 Compounds, 493 (2010) 202-207.
629 [53] M.A. Qamar, S. Shahid, M. Javed, M. Sher, S. Iqbal, A. Bahadur, D. Li, Fabricated novel
630 g-C_3N_4/Mn doped ZnO nanocomposite as highly active photocatalyst for the disinfection of
631 pathogens and degradation of the organic pollutants from wastewater under sunlight radiations,
632 Colloids and Surfaces A: Physicochemical and Engineering Aspects, 611 (2021) 125863.
633 [54] M.A. Qamar, S. Shahid, M. Javed, S. Iqbal, M. Sher, A. Bahadur, M.M. Al-Anazy, A.
634 Laref, D. Li, Designing of highly active g-C_3N_4/Ni-ZnO photocatalyst nanocomposite for the
635 disinfection and degradation of the organic dye under sunlight radiations, Colloids and Surfaces
636 A: Physicochemical and Engineering Aspects, 614 (2021) 126176.
637 [55] A. Balcha, O.P. Yadav, T. Dey, Photocatalytic degradation of methylene blue dye by zinc
638 oxide nanoparticles obtained from precipitation and sol-gel methods, Environmental Science
639 and Pollution Research, 23 (2016) 25485-25493.
640 [56] C. Xu, G.P. Rangaiah, X.S. Zhao, Photocatalytic Degradation of Methylene Blue by
641 Titanium Dioxide: Experimental and Modeling Study, Industrial & Engineering Chemistry
642 Research, 53 (2014) 14641-14649.
643 [57] L. Xiong, Y. Yang, J. Mai, W. Sun, C. Zhang, D. Wei, Q. Chen, J. Ni, Adsorption behavior
644 of methylene blue onto titanate nanotubes, Chemical Engineering Journal, 156 (2010) 313-320.

[58] W. Chu, W.K. Choy, T.Y. So, The effect of solution pH and peroxide in the TiO_2-induced photocatalysis of chlorinated aniline, Journal of Hazardous Materials, 141 (2007) 86-91.

[59] I.F. Waheed, M.A. Hamad, K.A. Jasim, A.J. Gesquiere, Degradation of methylene blue using a novel magnetic $CuNiFe_2O_4$/g-C_3N_4 nanocomposite as heterojunction photocatalyst, Diamond and Related Materials, 133 (2023) 109716.

[60] M.T. Shabbir, T. Hussain, S. Shakir, M. Anwar, A.H. Khoja, S. Nawaz, A.N. Satti, Enhancement in the photocatalytic and optoelectronic properties of erbium oxide by adding zinc oxide and molybdenum, Ceramics International, 49 (2023) 19691-19700.

[61] M.I. Din, R. Khalid, J. Najeeb, Z. Hussain, Fundamentals and photocatalysis of methylene blue dye using various nanocatalytic assemblies- a critical review, Journal of Cleaner Production, 298 (2021) 126567.